Applied Catalysis B: Environmental 314 (2022) 121492

Contents lists available at ScienceDirect

Applied Catalysis B: Environmental

journal homepage: www.elsevier.com/locate/apcatb

How H_2O may influence ambient CO oxidation over Au/BN

Tuyet-Mai Tran-Thuy [a,b,c], Teng-Li Yu [a], Shawn D. Lin [a,*]

[a] Department of Chemical Engineering, National Taiwan University of Science and Technology, Taipei 106, Taiwan
[b] Faculty of Chemical Engineering, Ho Chi Minh City University of Technology (HCMUT), Ho Chi Minh City, Viet Nam
[c] Vietnam National University Ho Chi Minh City, Ho Chi Minh City, Viet Nam

ARTICLE INFO

Keywords:
Ambient CO oxidation
Au/BN interfaces
Water co-catalyst
Water physisorption strength

ABSTRACT

Water is considered as a promoter for the CO oxidation over Au catalysts but experimental evidence of how adsorbed H_2O may influence the CO oxidation is scarce. In this study, Au/BN catalysts prepared by deposition method are subjected to calcination at different temperature. Increasing calcination temperature results in more Au particles distributed on BN basal plane, increased water affinity, increased defects on BN, and altered CO oxidation activity. All catalysts exhibit two CO adsorption bands at high relative humidity which are attributable to CO_{ad} on Au^0 and $CO(H_2O)_n$ species, although only a blue-shifted CO_{ad} is found at nominal dry condition. The turnover frequency is found to correlate with H_2O physisorption, with a volcano-shape dependency on surface density and first-layer physisorption enthalpy of H_2O_{ad}. How the physisorbed H_2O may influence CO oxidation over Au/BN is discussed and it implies that $(H_2O)_{n,ad}$ cluster is involved in CO activation.

1. Introduction

Low temperature CO oxidation is facile over supported nano-size gold catalysts following the numerous reports since the pioneer work by Haruta and coworkers [1–13]. The superior activity of Au catalysts for CO oxidation can be significantly suppressed by excess moisture which is an essential concern in applications for ambient and sub-ambient CO removal [14–17]. A small amount of water can enhance CO oxidation over oxide-supported Au catalysts, but the activity quickly deteriorates at above 30% relative humidity (RH) [14,16–18]. The enhancement role of water was reported in either re-activation of stable species like carbonate [19–21] or activation of O_2 [15–18] with the latter being more recently discussed and acknowledged. The recent study discussing Au_1/CeO_2 single atom catalyst [22] mentioned that carbonate species may not be the main cause for catalyst deactivation, which suggests that the water promotor role may not be related to carbonate species. The detrimental influence by excess moisture is generally attributed to surface flooding because that the activity can be recovered when excess moisture is removed [16,23]. However, the volcano-shape dependency of activity on moisture is vaguely explained by the balance of enhancement and suppression influences. To the best of our knowledge, no experimental result has been reported of how the surface density of adsorbed water or how the type of adsorbed water may influence the activity.

The role of adsorbed water may be relatively easier to be examined when using a more hydrophobic support for nano-size Au catalysts. In our previous work [24], we reported spectroscopic evidences of how water influences CO oxidation over Au/BN and the co-catalyst roles of water were discussed. The more hydrophobic Au/BN catalyst exhibits a monotonically increasing CO oxidation activity with RH. Surface species like $*CO(H_2O)_n$ and *OOH formed from interaction between CO_{ad} and H_2O_{ad} [24,25] and from proton transfer between H_2O_{ad} and O_{2ad} [16,24,26,27], respectively, are found and both are active toward CO_2 formation [24]. However, the type of H_2O_{ad} and how that H_2O_{ad} may result in the enhanced CO oxidation activity are not clear. It is likely that defects, including edge sites, of BN can provide adsorption sites for H_2O. Accordingly, in this study Au/BN is subjected to calcination at different temperature in order to change the defects and H_2O affinity. We found that increasing calcination temperature induced more physisorbed and chemisorbed H_2O but only physisorbed H_2O can be correlated to the observed CO oxidation activity. The nature of interaction between Au nanoparticles and BN support is discussed based on the results of in situ DRIFTS (diffuse reflectance infrared Fourier-transformed spectroscopy), X-ray photoelectron spectroscopy (XPS), X-ray absorption near edge structure (XANES), extended X-ray absorption fine structure (EXAFS), transmission electron microscopy (TEM) and scanning electron microscope (SEM) analyses.

* Corresponding author.
E-mail address: sdlin@mail.ntust.edu.tw (S.D. Lin).

https://doi.org/10.1016/j.apcatb.2022.121492
Received 26 October 2021; Received in revised form 3 April 2022; Accepted 20 April 2022
Available online 10 May 2022

2. Methods

2.1. Catalyst preparation

Two commercial h-BN materials were used as the support after calcination at 550 °C, named as BN1 (Alfa Aesar, 99.5%) and BN2 (Aldrich, 98%). Gold was loaded on h-BN at 1 wt% Au loading by a deposition method as previously reported [24]. The as-prepared Au/BN catalyst was calcined under 20% O_2 (balanced with He) flow at 300, 450, or 600 °C, respectively, for 1 h which temperature was coded as a suffix, e.g. Au/BN1-300, Au/BN2-600. The as-prepared non-calcined catalysts were coded without suffix.

2.2. Characterization

An inductively coupled plasma-atomic emission spectrometer (ICP-AES, Horiba Jobin Yvon, JY 2000–2) was used to analyze gold loading on h-BN based on the filtrate collected from Au/BN preparation. From ICP-AES results, all catalysts were confirmed an Au loading of 1.00 ± 0.03 wt%.

XRD (X-ray powder diffraction) was performed using beamline BL01C at the National Synchrotron Radiation Research Center (NSRRC), Hsinchu, Taiwan. The electron storage ring was operated at 1.5 GeV with a beam current of 200 mA. The XRD pattern was recorded by using a wavelength of 0.5167 Å at room temperature. The recorded diffraction was corrected to that of Cu $K_{\alpha1}$ radiation at a wavelength of 1.5418 Å. Graphitization index of BN was calculated from ratio of [Area (100) + Area (101)] and Area (102) for analysis of turbostratic defects [28] of h-BN and Au/BN.

TEM images were recorded using a Philips FEI Tecnai F30 HRTEM with an acceleration voltage of 200 kV. Sample was prepared by dropping 10 μl of catalyst suspension in ethanol on carbon-coated grid (300 mesh). The number-averaged Au particle size was calculated by averaging over 100 particles in the recorded images.

A commercial instrument (BELSORP-max) was used for measuring N_2 adsorption at −196 °C and water vapor adsorption at 30 °C. Samples were degassed under high vacuum at 200 °C for 12 h. A dual-isotherm method was applied for water vapor adsorption analysis wherein an evacuation at < 0.01 kPa for 4 h was carried out in between the 1st and the 2nd water adsorption measurement. The uptake difference between the two isotherms was used for chemisorption analysis while the uptake in the 2nd isotherm was used for physisorption analysis [24]. Langmuir model was used to fit H_2O chemisorption uptake as much as possible. However, the uptake data of some samples did not present the trend of approaching saturated uptake as Langmuir model does; these data were fitted with Henry's law, the approximate form of Langmuir model at low surface coverage. The physisorption uptake was fitted with BET model equation to extract monolayer coverage and the first-layer adsorption strength.

XPS (X-ray photoelectron spectroscopy) analysis was carried out with a commercial instrument (Thermo, Theta Probe). The binding energy from wide scan spectrum was calibrated with B 1 s at 190.7 eV. The scan with high resolution around Au 4 f, B 1 s, N 1 s and O 1 s were recorded to obtain detail information of surface components.

The Au L_{III} edge X-ray absorption spectroscopy of the catalysts was measured in transmission geometry at Beamline 17 C of the National Synchrotron Radiation Research Center (NSRRC), Taiwan, with a storage ring energy of 1.5 GeV. The energy was scanned from 200 eV below to 1200 eV above the Au L_{III} edge. EXAFS (extended X-ray absorption fine structure) data analysis was carried out using ATHENA and ARTEMIS programs with k2 weighting. Data in the k range from 3 to around 15 $Å^{-1}$ and that in the r range from 1 to 4 Å were used for analysis. Reference files were obtained from theoretical calculation employing the FEFF code for atom pairs such as Au–O, Au–Cl, and Au–Au. Reference materials, Au foil, $AuCl_3$ (Aldrich) and $Au(OH)_3$ (Aldrich) were used to check the consistency of calculated references.

DRIFTS (diffuse reflectance infrared Fourier-transformed spectroscopy) measurements were carried out using an in situ cell (Harrick, Praying Mantis, with ZnSe window) and Nicolet 6700 FTIR spectrometer with a mercury-cadmium-telluride (MCT/A) detector. The catalyst was loaded and pretreated, then cooled down to RT under N_2 purge. Thereafter, a background spectrum was taken using an accumulation of 64 scans and 4 cm^{-1} of resolution. The reactant flow was introduced at the same conditions as CO oxidation reaction test with/without saturated water vapor (~100% RH). CO gas phase signal was recorded with 1% CO in N_2 over low surface area quartz powders and was subtracted from the recorded spectrum over h-BN and Au/BN.

Raman spectra were collected on a UniRAM micro-Raman spectrometer with laser excitation (λ = 532 nm) to observe the effect of calcination temperature on the mode shift of E_{2g} vibration of BN.

2.3. CO oxidation tests

The CO oxidation reaction was conducted at 1% CO + 20% O_2 with different moisture partial pressures (balanced with He) in a flow-type packed-bed microreactor system operated at atmospheric pressure. The reaction temperature was controlled at 25 °C, designated as RT. Water was introduced by using a syringe pump into a heated feeding line for mixing with reactant flow. The reactor effluent was analyzed using an in-line GC with PDHID detector and packed columns of Porapak N and 5 A Molecular Sieve. The effluent analysis typically showed a carbon balance of 100 ± 5% with respect to the feed stream. The apparent reaction rate was calculated using a differential reactor model equation while the kinetic rate was evaluated by measuring changes of CO conversion versus space time. The turnover frequency (TOF) was then calculated based on the kinetic rate and calculated dispersion D. We evaluated dispersion by three approaches. The first used the equation $D = (6v_m/a_m)/d_s$ [29] based on particle size distribution from TEM analyses, where d_s is the surface-area mean diameter, v_m and a_m are the volume and the surface area of polycrystalline particles [29]. The second and the third approaches utilized the equation $D = 1/d_{Au}$, where d_{Au}(nm) was, respectively, the number-averaged particle size of Au particles from TEM analysis and the average particle size based on Scherrer equation and Au(111) peak width in XRD analyses. All three approaches led to TOFs showing similar trends. We reported the TOFs from approach 1 in the manuscript while those from the other two approaches in Supporting Information.

3. Results

3.1. Influence of H_2O on CO oxidation over Au/BN

Fig. 1 shows the influence of moisture concentration on the apparent reaction rate of differently pretreated Au/BN catalysts for RT CO oxidation, wherein two commercial BNs were used for catalyst preparation and the different calcination temperature was indicated and named by suffix. The apparent activity monotonically increased with increasing water partial pressure, from nominal dry to 100% RH, over all Au/BN catalysts. All Au/BN catalysts, except Au/BN1–300, showed a plateau activity at above 80% RH. This demonstrates a maximum moisture-enhancement of CO oxidation activity over each Au/BN catalysts, with no obvious activity suppression by the presence of excess moisture. Most oxide-supported Au catalysts exhibit a volcano-shape moisture dependency for CO oxidation activity, with a maximum activity typically occurring at around 30% RH [14,16,18]. Only a recent report by Dien et al. demonstrated a similar monotonic moisture-dependent CO oxidation over Au catalysts prepared by co-grinding organo-Au precursor and K-O-t-Bu with oxide support [30]. No CO_2 formation was found with CO-H_2O feed in the absence of O_2 at RT in DRIFTS and in microreactor analysis. This confirms that the observed activity comes from CO oxidation, not water gas shift reaction.

Fig. 1 also shows that the CO oxidation activity of Au/BN is

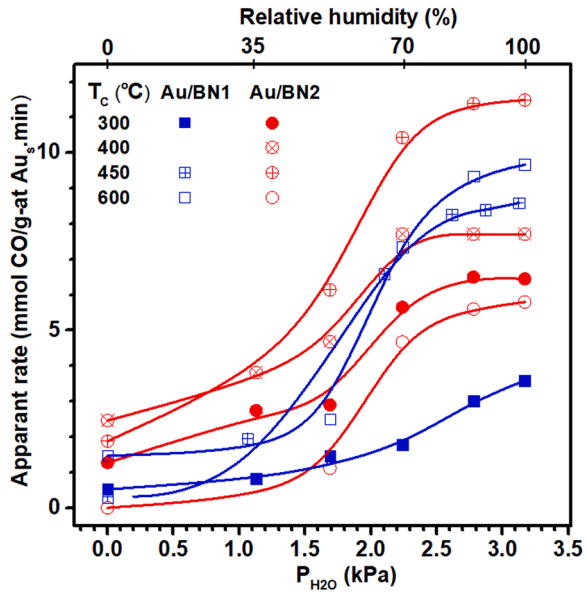

Fig. 1. Influence of moisture concentration on CO oxidation over differently pretreated Au/BN catalysts at RT and a space velocity of 163.7 and 233.8 μmol CO/g catalyst.min for Au/BN1 and Au/BN2, respectively.

influenced by catalyst calcination temperature. The two series of Au/BN catalysts using different BN exhibited somewhat different trends. For Au/BN1 catalysts, the CO oxidation activity at high RH followed: Au/BN1–300 < Au/BN1–450 ≤ Au/BN1–600, while for Au/BN2 it was Au/BN2–600 < Au/BN2–300 < Au/BN2–400 < Au/BN2–450. Obviously, the source of BN also influenced the CO oxidation activity in that Au/BN2–450 was more active than Au/BN1–450 and that the influence of calcination temperature on activity was somewhat different. This may be related to the defect sites on BN which can influence the dispersion of Au and/or H_2O adsorption. We will discuss the possible influences later.

In order to determine kinetic rate, the RT CO oxidation at high RH (80 ± 5%) was measured at varying space velocity as shown in Fig. S1. Although the recorded data scattered due to certain moisture condensation inside the reactor, the linear slope at low conversion range was used to calculate the kinetic rate. On the other hand, the RT CO oxidation at nominal dry condition was under differential reaction conditions, from which the kinetic rate was directly calculated. The TOF (turnover frequency) of Au/BN catalysts was calculated based on the Au dispersion estimated from the average Au particle size from TEM (Fig. S2 and Table 1). Table 1 shows comparison of the TOF of all Au/BN catalysts and with literature data. The TOF of these Au/BN catalysts at high RH (around 80%) are in the range of 0.05–0.18 s^{-1}, in the same range as that of the most active oxide-supported Au catalysts [22,30–34]. Au/BN2–450 catalyst showed the highest TOF of RT CO oxidation at high RH among these Au/BN catalysts. Changing calcination temperature led to changes in TOF by a factor of around 3 but relatively insignificant difference in Au particle size was found (Table 1).

To study how water might have influenced the CO oxidation activity of Au/BN at high RH, water adsorption analysis was carried out using a dual isotherm method. Fig. 2 shows the isotherms of Au/BN1 and Au/BN2 catalysts, wherein the isotherms of h-BN supports are included for comparison. The overlapping first and second water adsorption isotherms of both h-BN1 (Fig. 2a) and h-BN2 (Fig. 2b) indicate the absence of chemisorbed (irreversibly adsorbed) H_2O; only physisorbed (reversibly adsorbed) H_2O was presented on as-received h-BN supports. With Au loading on h-BN, the H_2O uptake became higher than that on h-BN support with an increasing trend with increase of calcination temperature. Furthermore, the chemisorbed H_2O (the difference between the 1st and the 2nd isotherms) became more significant with increasing calcination temperature (Fig. S3). This indicates that certain strong water

Table 1
TOF of RT CO oxidation over Au/BN, comparing to other Au metal oxide catalysts.

Catalyst	Au particle size[a] (nm)			Dispersion[a]	TOF[a] (10^{-3} s^{-1})		Ref.
	d_{Au} (111)	d_{Au}	d_s		~ 0% RH	~ 80% RH	
Au/BN1–300	8.0	4.1 ± 0.5	4.6	0.25	9.8	46.1	This work
Au/BN1–450	9.3	3.4 ± 0.5	4.0	0.29	nil	81.3	
Au/BN1–600	9.4	3.7 ± 0.8	4.5	0.26	28.3	95.3	
Au/BN2–300	10.2	3.7 ± 0.6	4.2	0.28	23.0	72.2	
Au/BN2–400	–	3.5 ± 0.7	4.2	0.28	44.7	91.6	
Au/BN2–450	6.7	3.1 ± 0.6	4.1	0.28	34.0	172.8	
Au/BN2–600	8.3	3.9 ± 0.8	5.5	0.21	nil	86.4	
0.94% Au/Al_2O_3	–	2.4 ± 1.1			20[b]	–	[31]
2% Au/TiO_2	–	1.7 ± 0.4			60[b]	–	
1.8% Au/TiO_2	–	2.7 ± 0.6			120[c]	–	[33, 34]
0.7% Au/TiO_2	–	3.1 ± 0.7			30[c]	–	
1% Pd (DF)/Fe_2O_3	–	2.0			–	50[d]	[35]
3.15% Au/FeO_x	6.5	–			130[e]	–	[32]
1% AuTFA/TiO_2	–	2.6			114[f]	57	[30]
1% AuTFA/K-SiO_2	–	2.3			41[f]	69	
0.03% Au_1/CeO_2	–	–			–	200[g]	[22]
0.98% Au/CeO_2	–	~5			36[g]	–	

[a] Au particle size was $d_{Au(111)}$: based on Scherrer equation and Au(111) peak width in XRD, d_{Au}: number-averaged particle size from TEM, and d_s: area-averaged diameter of Au particles [29]. Dispersion was calculated based on Dispersion $D = (6.v_m/a_m)/d_s$ [29] using d_s, from which TOF was calculated.
[b] CO oxidation at 0 °C, 1% CO + 20% O_2.
[c] CO oxidation at 27 °C, 1% CO + 20% O_2.
[d] CO oxidation at 20 °C, 0.01% CO + 1% O_2, balance N_2.
[e] CO oxidation at 30 °C, 1 kPa P_{CO}, 1 kPa P_{O2}, 75 kPa P_{H2}, balance N_2.
[f] CO oxidation at 30 °C, 500 ppm CO + 20% O_2; TOF calculated from the reported conditions and differential reactor equation although the conversion was in the range of 60% and above.
[g] CO oxidation at 24 °C, 1 vol% CO + 1 vol% O_2, with/without ~ 60% RH, balance He.

adsorption sites were generated with increasing calcination temperature of Au/BN.

The H_2O chemisorption uptake was fitted with equations of Langmuir model (for Au/BN1–450, Au/BN1–600, Au/BN2–600) and of Henry's law (for Au/BN1–300, Au/BN2–300 and Au/BN2–450) (Fig. S4). The H_2O physisorption (the 2nd isotherm in Fig. 2) was fitted with BET model. The fitting results from physisorption and chemisorption are shown as lines in Fig. 2 and in Table 2. Among these samples, the chemisorption uptake of Au/BN1–450, Au/BN1–600 and AuBN2–600 could be fitted with Langmuir model, for which nondissociative molecular adsorption Langmuir equation could fit the data while dissociative adsorption Langmuir equation could not (Fig. S4). The fitting results in Table 2 indicate that H_2O adsorption strength of both chemisorbed and physisorbed H_2O increased with increasing Au/BN

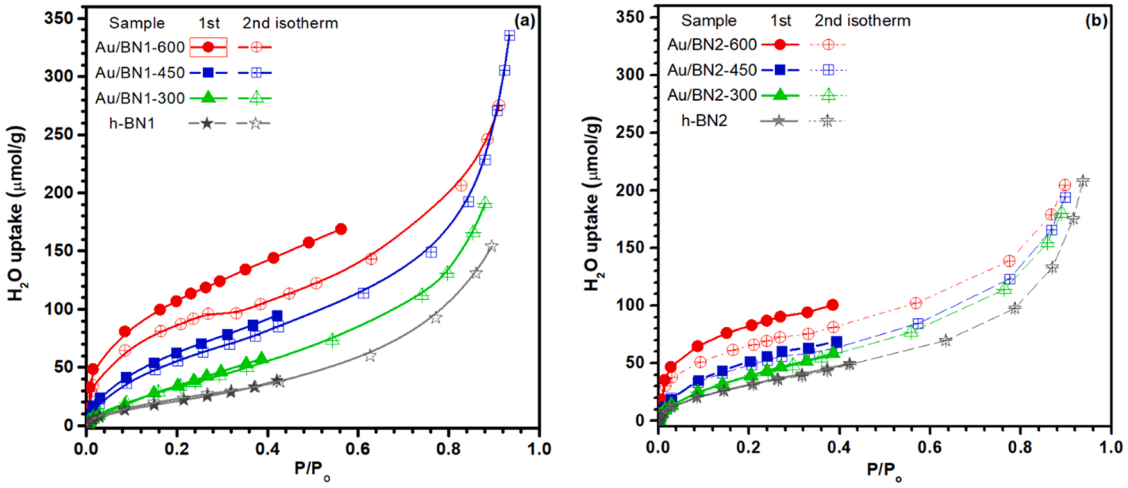

Fig. 2. Water adsorption isotherms of (a) h-BN1 and Au/BN1, and (b) h-BN2 and Au/BN2 catalysts at 30 °C. A dual isotherm method was applied, of which the 1st isotherm is represented by solid symbols while the 2nd isotherm is represented by open symbols. Lines represent the fittings using model equation (see text for details).

Table 2
N_2 and H_2O adsorption analysis of Au/BN1 and Au/BN2 catalysts and BN supports.

Sample	BET	H_2O Physisorption		H_2O Chemisorption		Ref.
	S.A (m^2/g)	C_{H2O}	$N_{1,H2O}$ (μmol/g)	K (kPa^{-1})	N_0 (μmol/g)	
h-BN1–550	8.0 ± 0.2	15.1 ± 0.8	23.3 ± 1.6	–	–	This work
Au/BN1–300	8.5 ± 0.2	9.1 ± 0.2	38.3 ± 1.1	2.2 ± 0.4	–	
Au/BN1–450	14.5 ± 0.1	16.6 ± 1.3	54.6 ± 5.3	19.2 ± 1.5	7.1 ± 0.4	
Au/BN1–600	13.6 ± 0.1	42.7 ± 4.7	75.1 ± 9.2	37.5 ± 3.5	20.5 ± 1.1	
h-BN2–550	17.1 ± 0.1	17.5 ± 0.9	30.1 ± 1.7	0.9 ± 0.1	–	
Au/BN2–300	16.7 ± 0.1	14.2 ± 0.2	39.2 ± 0.8	0.9 ± 0.1	–	
Au/BN2–450	18.4 ± 0.1	28.9 ± 0.8	43.3 ± 1.4	3.8 ± 0.1	–	
Au/BN2–600	17.3 ± 0.1	48.4 ± 4.4	56.3 ± 5.7	7.9 ± 0.1	18.9 ± 0.6	
TiO_2 (Rutile)-250	10.0	–	89	–	–	[24, 36](*)
TiO_2 (Rutile)-600	9.4	–	92	–	–	
α-Fe_2O_3-250	21.2	–	172	–	–	
α-Fe_2O_3-600	20.0	–	212	–	–	

S.A: specific surface area (m^2/g), calculated from N_2 adsorption.
N_1: monolayer uptake of physisorption, from fitting with BET equation.
N_o: monolayer uptake of chemisorption, from fitting with Langmuir model.
C_{H2O}: H_2O physisorption parameter, from fitting with BET equation.
K_{H2O}: H_2O adsorption constant, from fitting with Henry or Langmuir model.
(*): H_2O adsorption on TiO_2 and Fe_2O_3 was conducted at 18 °C and 25 °C, respectively.

calcination temperature, as indicated by K_{H2O} and C_{H2O}, respectively. Also, the monolayer uptake (N_1) from physisorbed H_2O fitting shows an increasing trend with calcination temperature (Table 2). The calcination treatment likely resulted in Au-BN interfacial sites and/or defect sites that enhanced both physisorption and chemisorption of H_2O on Au/BN catalysts.

Crystalline BN is well known to be hydrophobic. The H_2O uptake measured on h-BN and Au/BN was relatively low, approximately 30% that of oxide surface when physisorbed monolayer uptake (N_1) was normalized by BET area (Table 2), which confirmed the more hydrophobic surface of BN. Comparing the two h-BN supports, h-BN2 had a higher BET surface area, a lower BET-normalized N_1, and a slightly higher affinity to H_2O (indicated by C_{H2O}), than BN1. The reason of such a difference is not known at this moment although the water uptake on Au/BN can be associated to defect sites which will be discussed later.

We analyzed the possible correlation between CO oxidation TOF of Au/BN catalysts and their H_2O affinity considering both adsorption strength and uptakes. A possible correlation of TOF was found with respect to physisorbed H_2O as shown in Fig. 3. Noticeably, Fig. 3a shows that TOF of all Au/BN catalysts increased with BET-normalized-uptake (per m^2) of physisorbed H_2O based on uptakes at P/P_0 ~0.01 and 0.8, respectively, representing nominal dry and high RH (~80%) conditions; the highest uptake data in Fig. 3a seems indicating an activity suppressed by high H_2O uptake. Not only physisorbed H_2O uptake seems influencing the TOF but also the physisorption strength. Fig. 3b shows a volcano shape dependency of TOF versus H_2O physisorption strength based on C_{H2O} from BET model fitting. The correlation of TOF @ ~80% RH is more obvious than that at nominal dry conditions. This correlation suggests a promotional role of physisorbed H_2O in RT CO oxidation over Au/BN which will be discussed below.

3.2. *Influence of H_2O on CO adsorption over Au/BN*

Fig. 4 shows the DRIFTS spectra of CO adsorption on Au/BN1 and Au/BN2 under nominal dry and ~100% RH conditions. h-BN supports showed no CO adsorption in dry and wet conditions. Au/BN1–300 exhibited an absorbance at 2113 cm^{-1}, under dry condition, corresponding to CO adsorption over metallic Au [24,37,38]. Increasing calcination temperature lead to a blue shift in ν_{CO} band from 2113 to 2146 cm^{-1} over Au/BN1 catalysts and from 2132 to 2150 cm^{-1} over Au/BN2 catalysts. The blue-shifted CO absorbance was typically attributed to the CO_{ad} on oxidic Au sites [4,39–41]. The attribution to oxidic Au sites is not consistent with the main Au^0 state observed in XPS and XANES analyses as that will be shown later. Interestingly, two ν_{CO} bands at 2113 and 2170 cm^{-1} were found over all Au/BN catalysts under high RH, regardless of the different ν_{CO} band position under nominal dry condition. This suggests a certain interaction might have led to the blue shift of CO_{ad} observed at nominal dry condition and moisture could interrupt such interaction. The observed blue shift at nominal dry

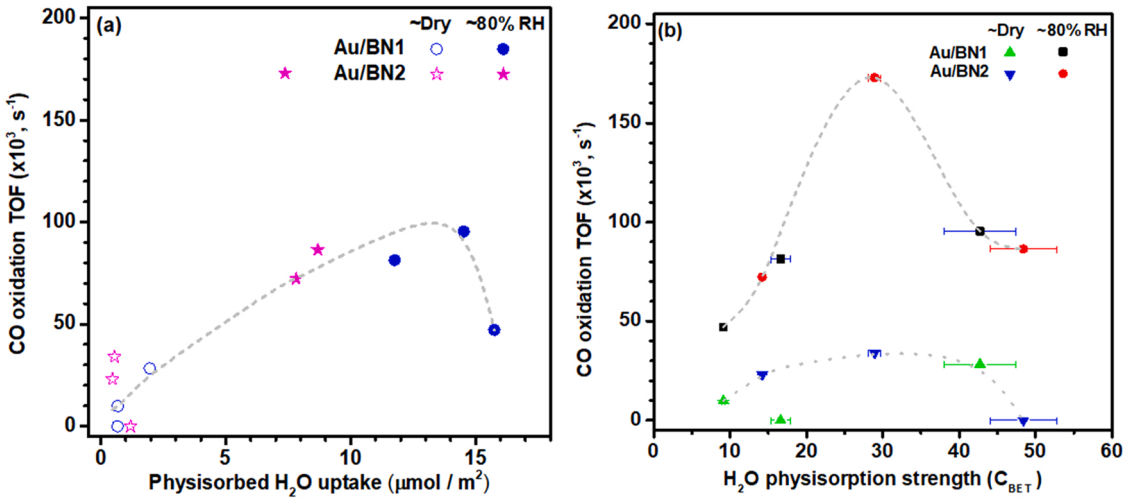

Fig. 3. Correlation of the TOF of Au/BN for RT CO oxidation (a) with respect to physisorbed H_2O uptake per m^2 BET surface area, and (b) with respect to H_2O physisorption strength, i.e., C parameter of BET equation. The water uptake was taken at $P/P_0 = 0.01$ and 0.8, respectively, for nominal dry and high RH conditions. Gray lines are provided for showing the trends.

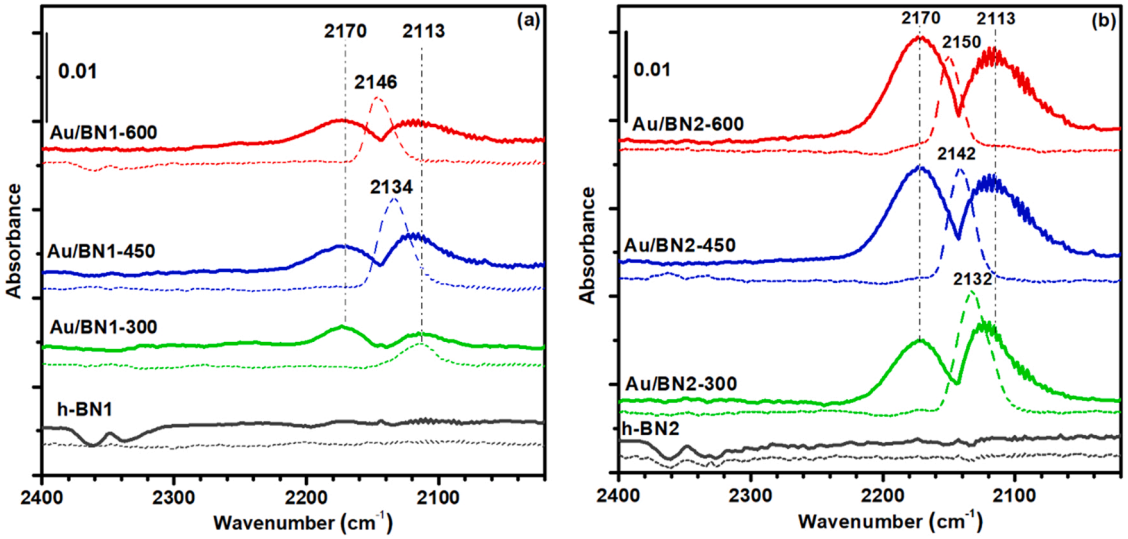

Fig. 4. In situ DRIFTS of CO adsorption over (a) h-BN1 and Au/BN1 catalysts and (b) h-BN2 and Au/BN2 catalysts under nominal dry (dot line) and 100% RH (solid line) conditions at RT.

condition is attributed to CO_{ad} interaction with defect sites on BN at Au-BN interface and H_2O_{ad} on defect sites on BN broke the CO_{ad} interaction. The DRIFTS results also indicate that all Au/BN in this study contained the same types of surface CO at high RH. The 2113 cm^{-1} band is obviously the CO adsorbed on Au^0 while the 2170 cm^{-1} was interpreted previously as $CO(H_2O)_n$ species [24,25] representing adsorbed CO with H_2O interaction. The DRIFTS results also indicate that the different TOF of these Au/BN catalysts (Table 1) cannot be attributed to the seemingly different Au oxidation state suggested by blue-shifted CO_{ad} at nominal dry condition. This supports that Au^0 sites are responsible for the observed CO oxidation reaction wherein moisture may have played a promoting role.

3.3. Characterization of Au/BN

The Au oxidation state was analyzed using XANES and XPS. XANES of Au/BN catalysts are shown in Fig. 5, indicating that Au was mainly in reduced metallic state. The EXAFS (Fig. S6) fitting results of Au/BN1 catalysts in Table 3 show a fitted metallic Au-Au coordination number of around 8.5 regardless of the calcination temperature. The fitting results can correspond to an average particle size in the range 2–5 nm [42–44], consistent with TEM analysis. These results indicate that Au/BN catalysts had mainly Au^0 at high dispersion state, which was not significantly changed by calcination temperature.

The XPS results of Au/BN catalysts are shown in Figs. S7, S8 and Table 4. There was no strong evidence of increasing Au oxidation state with increasing calcination temperature, in consistent with XANES results; however, the slightly shifted Au 4 $f_{7/2}$ peak, which was more obvious with Au/BN1, implies the presence of a small fraction of $Au^{\delta+}$ state which might be resulted from charge transfer effect between Au and defects of BN [38].

The EXAFS fitting results of Au/BN indicate Au^0 nanoparticles of an average size of 2–5 nm are presented. TEM images of Au/BN catalysts (Fig. 6) show that Au particles of mainly 2–5 nm size distributed on BN support. Based on the particles size distribution (Fig. S2), the calculated number-average particles sizes are listed in Table 1 wherein the particles sizes calculated from synchrotron-XRD (Fig. 7) are included for comparison. There was no obvious evidence that the average Au particle size

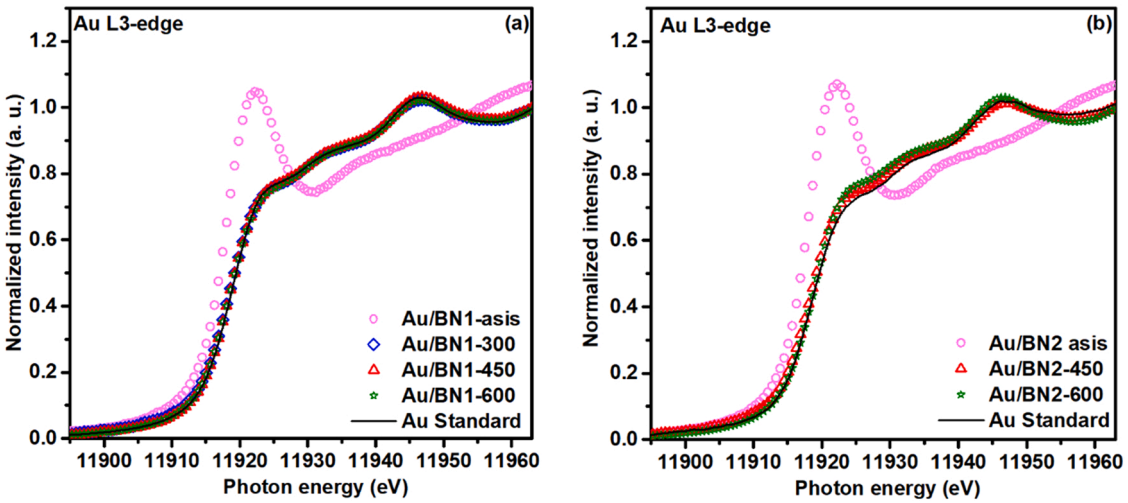

Fig. 5. Au L3-edge XANES of Au/BN catalysts, wherein Au/BN-asis indicates the non-calcined catalysts.

Table 3
EXAFS fitting results of Au/BN1 catalysts.

Catalysts	Shell	R (Å)	CN	σ^{2*} 10^3	R-factor
Au/BN1–300	Au-Cl	2.364 ± 0.008	0.3 ± 0.1	7.0 ± 0.6	0.005
	Au-Au	2.858 ± 0.006	7.3 ± 0.7		
Au/BN1–450	Au-Au	2.843 ± 0.004	8.6 ± 0.6	8.5 ± 0.6	0.007
Au/BN1–600	Au-Au	2.845 ± 0.003	8.6 ± 0.5	8.9 ± 0.6	0.006

Table 4
XPS analysis of h-BN and Au/BN catalysts.

Sample	Au $4f_{7/2}$ (eV)	Au/B	N/B	O/B
h-BN1–550	–	0	1.4	0.06
Au/BN1–300	84.4	0.01	1.3	0.09
Au/BN1–450	84.4	0.03	1.3	0.04
Au/BN1–600	84.4	0.06	1.4	0.05
h-BN2–550	–	0	0.93	0.15
Au/BN2–300	84.1	0.01	0.93	0.12
Au/BN2–450	84.1	0.02	1.0	0.10
Au/BN2–600	84.1	0.01	1.1	0.16

was influenced by increasing calcination temperature. For Au/BN1–300, most Au particles distributed along the edge of BN planes as reported previously [24]. Increasing calcination temperature resulted in more Au particles distributed on BN basal plane, without significant sintering. The results suggest the migration of Au particles to the defect sites on BN planes caused by calcination, in consistent with the weak interaction between Au cluster and BN revealed by DFT analysis [25]. The nano-size Au seems stable on BN as that the TEM images of spent Au/BN2–450 (Fig. S5) indicated only a slight increase in averaged Au particle after a week-long RT CO oxidation test at high RH ~80%. XRD patterns, analyzed using synchrotron light source, are shown in Fig. 7. The XRD peak shape of Au (111) showed a sharp peak on top of a broad base peak (Fig. S9), indicating the presence of both large and small Au particles. This may have resulted in that the calculated Au particle size from XRD Au (111) peak width is typically larger than that from TEM image analysis (Table 1). TEM images also showed a relatively small fraction of Au particles larger than 10 nm.

The surface composition calculated from XPS (Table 4) indicates a small change in Au/B molar ratio, related to Au dispersion on BN surface, of Au/BN1 by increasing calcination temperature, but it was not obvious with Au/BN2. We noted earlier that the H_2O adsorption sites should be related to the defects and edge sites of BN plane. The XPS B 1 s and N 1 s of Au/BN catalysts were found shifted slightly to higher binding energy with increasing calcination temperature (Fig. S7, S8), supporting the claim of more oxidized defect/edge sites with increasing calcination temperature. However, the O/B and N/B composition ratios (Table 4) did not show a clear trend with increasing calcination temperature.

Scanning electron microscopy (SEM) images (Fig. S10) show that h-BN1 and h-BN2 were both of slab shape with h-BN1 having a larger slab dimension than h-BN2. Loading Au did not change the slab shape of h-BN but Au/BN1–450 and Au/BN1–600 showed an increased number of smaller slabs comparing to h-BN1 and Au/BN1–300. This may explain changes in BET specific area of Au/BN1 catalysts with calcination temperature in Table 1. The BN slab dimension of Au/BN2 catalysts was not significantly changed by increasing calcination temperature, corroborating their similar BET specific area (Table 1). The synchrotron-XRD revealed no shift in the two theta of BN (102) diffraction peak and its band width when comparing BN support with the prepared differently calcined Au/BN. Graphitization index (GI) is frequently used to express the relative concentration of the turbostratic stacking faults of BN, with a GI of 1.6 representing perfect 3-D ordering and a GI of 50 as the upper limit of disordered turbostratic structure [28]. The Au/BN1 catalysts showed an increased GI, of 2.0, 2.9, and 3.4, respectively, with increasing calcination temperature from 300, 450, to 600 °C. On the other hand, Au/BN2 catalysts showed a similar GI, 2.9, 3.0, and 2.9, respectively, with increasing calcination temperature. This corroborates the more significant increase in physisorbed H_2O monolayer coverage ($N_{1,\ H2O}$ in Table 2) and H_2O adsorption strength by increasing calcination temperature of Au/BN1 comparing to Au/BN2. This suggests that increasing calcination temperature resulted in an increased density of defect/edge sites on BN which consequently influenced H_2O uptake and subsequently the CO oxidation activity of Au/BN catalysts.

4. Discussion

The Au/BN catalysts prepared in this study contain well dispersed Au^0 nanoparticles over BN support regardless of source of BN and the calcination temperature. The Au metallic state is confirmed by both XANES and XPS. The Au dispersed state is identified using TEM and synchrotron XRD, indicating insignificant influence of Au particle size by increasing calcination temperature. However, the IR band of CO_{ad} at nominal dry shows an increasing blue shift with increasing calcination temperature. This can be attributed to that CO adsorption preferentially occurs on Au near its interface with BN. At the interface, the adsorbed CO is probably stabilized via interaction with defect sites on BN, which can lead to the observed blue shift of CO_{ad} vibration band. The increasing defect sites on BN support with increasing calcination

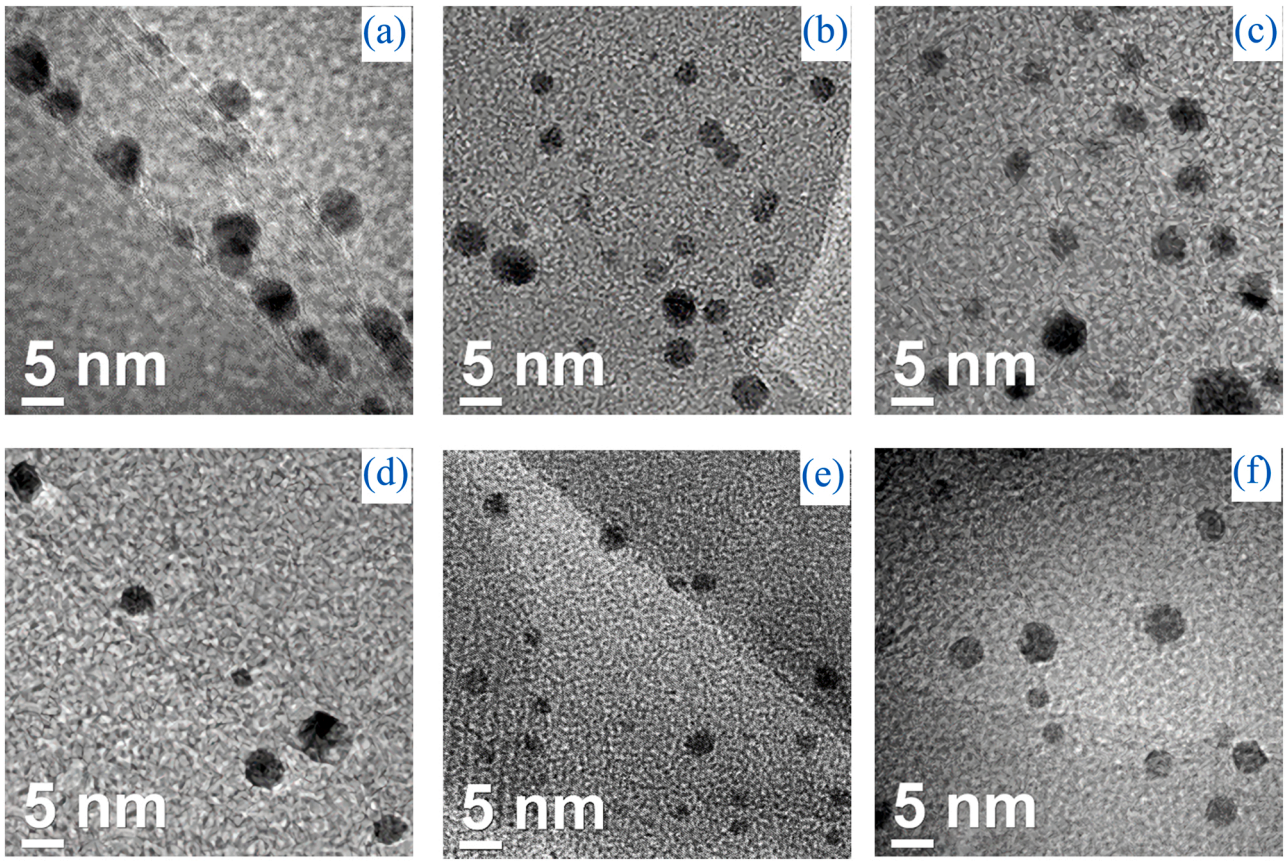

Fig. 6. TEM images of (a) Au/BN1–300, (b) Au/BN1–450, (c) Au/BN1–600, (d) Au/BN2–300, (e) Au/BN2–450, and (f) Au/BN2–600.

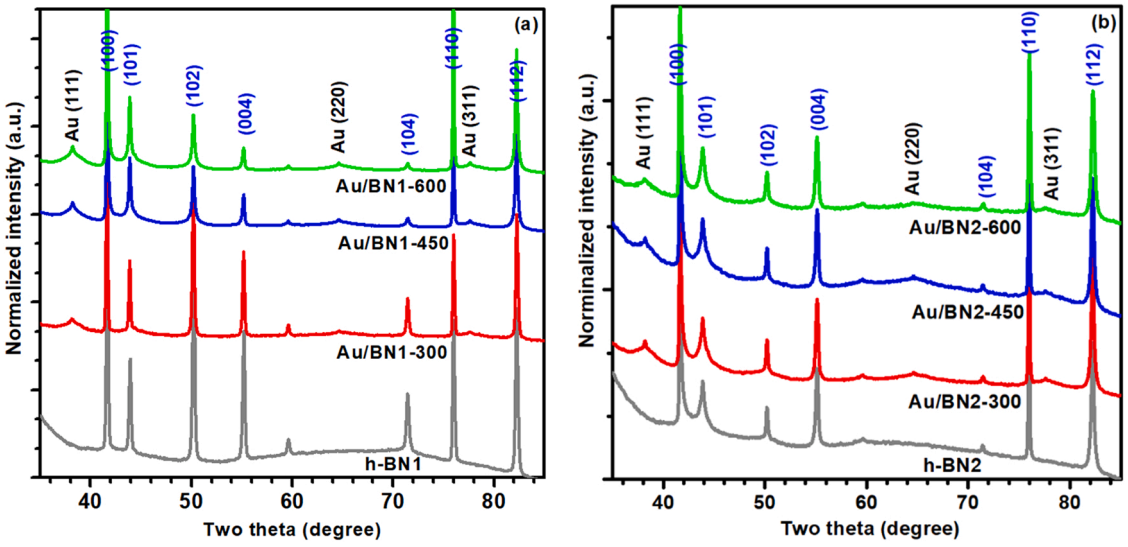

Fig. 7. XRD patterns of (a) h-BN1 and Au/BN1 catalysts, and (b) h-BN2 and Au/BN2 catalysts using synchrotron light source. The diffraction signal intensity of different samples was normalized with respect to h-BN (100) at 41.7°.

temperature is indicated by the more oxidized B 1 s and N 1 s in XPS and also by the increased GI from XRD. BN basal plane is hydrophobic. Quiller et al. [45] reported that H_2O is scarcely adsorbed (chemisorbed and physisorbed) on both metallic and oxidic gold phases. Consequently, the increasing H_2O chemisorption and increasing physisorption affinity with increasing calcination temperature is expected to be associated with the defect sites on BN. When CO is coadsorbed with H_2O the blue-shifted CO_{ad} band disappears which can be attributed to that the defect sites become occupied by H_2O. As a result, the CO becomes molecularly adsorbed CO_{ad} on Au surface, explaining the observed 2113 cm^{-1} band [46], and also that associated with H_2O as $CO(H_2O)_n$, explaining the 2170 cm^{-1} band [24]. Fu et al. illustrated by DFT modeling that CO coadsorbs as $CO(H_2O)_n$ is more stable than as CO_{ad} on Au_9 cluster on BN [25].

Both chemisorbed and physisorbed H_2O were found increased with increasing calcination temperature but only physisorbed H_2O was found

to correlate with CO oxidation activity. We have no evidence to conclude the possible role of chemisorbed H_2O. It is suspected that the chemisorbed H_2O passivated the defect sites on BN that caused the observed blue-shifted CO_{ad} band at nominal dry condition, leading to the reverse of blue-shifted CO_{ad} band back to 2113 cm^{-1}. This will need further verification. A recent study [13] examined H_2O_{ad} over $Au/TiO_2(110)$ using TPR and both physically and dissociatively adsorbed H_2O were identified based on the observed desorption peak at ~360 and ~510 K. The results indicate a much stronger binding strength of chemisorbed H_2O than physisorbed H_2O. Although TiO_2 support and BN support have distinguishable difference, it can be expected the strong binding strength may result in that chemisorbed H_2O becomes just a spectator during room temperature CO oxidation over Au/BN. DFT modeling shows that the physisorbed H_2O on BN may present as H_2O clusters. [25] The increased physisorption uptake may be due to increasing defect sites for physisorption and/or to increasing H_2O cluster size. Consequently, the $CO(H_2O)_{n,ad}$ may be formed at Au-BN interface as BN does not adsorb CO and Au surface has low H_2O uptake. Furthermore, the different C constant of these Au/BN catalysts from BET model fitting correspond to only a few kJ/mol difference in the first layer physisorption enthalpy, which may be associated with the different H_2O cluster size. Fu et al. [25] also reported that the adsorption energy of $CO(H_2O)_n$ on Au_9/BN and on Au_9 varied within a few kJ/mol range.

Fig. 3a suggests a near volcano shape dependency of RT CO oxidation TOF of Au/BN on the surface density of physisorbed H_2O_{ad} (per m^2), though with some data scattering. This type of volcano-shape dependency of CO oxidation activity on RH are previously reported over oxide-supported Au catalysts [14,16,17]. The decreasing activity at high RH is typically attributed to surface flooding by excess water on oxide surface [15,17]. However, it has not been interpreted in term of surface density of H_2O_{ad}. Fig. 3a suggests a maximum TOF occurring at near 15 μmol H_2O_{ad}/m^2, equivalent to an average of around 9 molecules/nm^2. With a cross-sectional area of 10.6 $Å^2$ [47], this corresponds well to a nearly monolayer coverage of surface. However, this monolayer coverage cannot be confirmed if we consider the possible formation of H_2O cluster.

Fig. 3b suggests that the first-layer H_2O physisorption enthalpy may also influence the CO oxidation activity. As discussed earlier, this may be due to the varying H_2O cluster size influencing the properties of CO $(H_2O)_{n,ad}$, which is reported as an active intermediate leading to facile CO oxidation over Au catalysts [24,25]. The HO_2 (protonated O_2) is considered as another active intermediate over Au catalysts [16,17,25,45]. Although the state of adsorbed water (cluster) may also influence the proton transfer between $(H_2O)_{n,ad}$ and $O_{2,ad}$, we do not have evidence in this study to discuss how H_2O_{ad} may influence this HO_2 intermediate. Fig. 3b shows that the influence of H_2O physisorption enthalpy is not obvious at nominal dry condition. This may be due to the low surface density of H_2O_{ad} resulting in an insignificant contribution of physisorbed H_2O. The volcano-shape dependency of TOF on H_2O adsorption strength at high RH suggests the determining role of physisorbed H_2O which may be governed by the change of H_2O cluster size.

In this study, BN defect sites are attributed to play a role for H_2O adsorption in addition to the role of stabilizing Au nanoparticles. It can be expected that defect sites on BN include edge sites, vacancies and hetero atoms of BN basal plane. Our XPS analysis identified O as the only hetero atom. Vacancies on BN basal plane and edge sites are expected to contain B- and N-terminal sites. In a recent study [48], vacancy defects of BN were found to spontaneously reduce several metal precursors to metal nanoparticles residing on defect sites. This supports our claim that Au nanoparticles can be stabilized by defects of BN. Recent DFT calculations also demonstrate that the interaction of Au with vacancy defected h-BN sheet is much stronger than that of free standing Au particles on h-BN sheet [49]. With increasing calcination temperature, more Au nanoparticles were found to distribute on BN basal plane (TEM). This implies that more defects were generated by increasing calcination temperature resulting in the redistribution of Au nanoparticles. Furthermore, GI analysis based on synchrotron XRD suggests an increasing extent of turbostratic stacking of BN with increasing calcination temperature, which also indicates increase in defects. We also performed Raman spectroscopy analysis of BN and Au/BN (Fig. S13). The results showed that the BN E2g band of Au/BN was red-shifted when compared to that of BN support. Also, increasing calcination temperature of Au/BN caused larger red shift. The red shift of E2g band of BN can be attributed to strain effect [50], oxygen intercalation [51] or the presence of dopant [52]. All these point to the possibility of increasing defect density of Au/BN by increasing calcination temperature. When ~2 nm Au particles (from TEM) resided on defects, the change of N/B ratio caused by defect formation may not be resolved in XPS due to its limited information depth. This may lead to the absence of law of N/B ratio of Au/BN in this study.

We do not have evidence to discuss the type of defects in this work. However, we would expect the same type of defects in different Au/BN samples because they were subjected to the same thermal energy driving force to a different extent. Lei et al. [48] reported that the defects of BN generated by cryogenic milling are mainly N-vacancies, with accompanying formation of –OH groups. This provides a reason of the presence of O as a hetero atom in our XPS analysis. The Au nanoparticles residing on such N-vacancies are reported to be around 2 nm, similar to the size of Au particles of our Au/BN.

There are more studies in the literature discussing the interaction between defects on BN sheet and metal atom (and metal clusters) but the discussion of H_2O adsorption on BN defects is scarce. As mentioned earlier, we did not observe CO_{ad} on BN. A recent review [53] on BN sheet on metal support also concludes the absence of CO_{ad} on BN sheet while H_2O cluster may reside on BN surface. This corroborates with our proposed model of CO_{ad} on Au and H_2O_{ad} mainly on BN. The presence of defects can be expected to possibly have interaction with metal nanoparticles and with adspecies. DFT calculations [54] suggest the presence of different direction of charge transfer of Au clusters on B vacancy (V_B) and on N vacancy (V_N). Our XPS analysis on Au 4 f demonstrates insignificant shift, suggesting either that the extent of charge transfer was relatively insignificant or that the sum of both directions of charge transfer was insignificant.

Oxide-supported Au catalysts are known to have a superior RT CO oxidation activity comparing to other supported metal catalysts, and a TOF of around 0.1 s^{-1} at nominal dry condition has been reported [30,33–35]. The active Au/BN at high RH in this study shows a CO oxidation TOF similar to that of the most active oxide-supported Au catalysts. This implies that a similar interfacial synergistic interaction may be involved in these supported Au catalysts. Au/BN catalysts can work well at high RH for RT CO oxidation which may find applications for ambient CO abatement and detection. The influence of calcination temperature on Au/BN is mainly via alternating the H_2O physisorption (Table 2), which may result in H_2O cluster changes significantly influencing the CO oxidation activity [25]. Moreover, the essential role of Au/BN interfacial sites in H_2O enhancement of RT CO oxidation over Au catalysts is strongly suggested by the results in this study.

5. Conclusions

The prepared Au/BN catalysts contains dispersed metallic Au particles mainly of 2–5 nm regardless of the source of BN support or the calcination temperature, as verified by XANES, EXAFS and TEM. Increase of calcination temperature results in more Au particles distributed on BN base plane, increased water affinity (both in uptakes and adsorption strength of physisorption and chemisorption), increased density of defects on BN, and noticeably altered CO oxidation activity at RT and high RH. All Au/BN catalysts in this study show an increasing CO oxidation activity with RH up to a plateau region at RH above 80%. The TOF at high RH is found to correlate with H_2O physisorption, with a volcano-shape dependency on first-layer physisorption strength and on

surface density of H_2O_{ad}. This is interpreted as possible formation of H_2O cluster interacting with CO_{ad}. DRIFTS analysis indicates blue-shifted CO_{ad} on Au sites at nominal dry condition which can be attributed to CO_{ad} at Au-BN interface having an interaction with defects on BN. At high RH, DRIFTS reveals two bands associated to CO_{ad} on Au^0 and CO $(H_2O)_n$ species, which can be rationalized by H_2O_{ad} on BN defect sites. The results of this study point to the important contribution of Au-BN interface sites where $CO(H_2O)_n$ can form from CO_{ad} on Au^0 and H_2O_{ad} on BN. The enhanced TOF at high RH can be attributed to the formation of $CO(H_2O)_n$ and H_2O_{ad} species that can possibly activate O_{2ad} on Au^0. The maximum TOF of Au/BN for RT CO oxidation at high RH is nearly the same as the most active Au catalysts reported in the literature.

CRediT authorship contribution statement

Tuyet-Mai Tran-Thuy: Conceptualization, Methodology, Investigation, Writing – original draft. **Teng-Li Yu:** XANES and EXAFS analysis. **Shawn D. Lin:** Conceptualization, Supervision, Writing – review & editing.

Declaration of Competing Interest

The authors declare that they have no known competing financial interests or personal relationships that could have appeared to influence the work reported in this paper.

Acknowledgments

The financial support from Ministry of Science and Technology (Grant numbers: MOST 110-2221-E-011-021), Taiwan is acknowledged. We thank Professor Toyoko Imae, Graduate Institute of Applied Science and Technology, National Taiwan university of Science and Technology, for allowing the uses of H_2O vapor adsorption facilities. Tuyet-Mai Tran-Thuy also acknowledges the support of time and facilities from Ho Chi Minh City University of Technology (HCMUT), VNU-HCM for this study.

Appendix A. Supplementary material

Supplementary data associated with this article can be found in the online version at doi:10.1016/j.apcatb.2022.121492.

References

[1] M. Haruta, T. Kobayashi, H. Sano, N. Yamada, Novel gold catalysts for the oxidation of carbon monoxide at a temperature far below 0C, Chem. Lett. 16 (1987) 405–408, https://doi.org/10.1246/cl.1987.405.
[2] S.D. Lin, M. Bollinger, M. Vannice, Low temperature CO oxidation over Au/TiO_2 and Au/SiO_2 catalysts, Catal. Lett. 17 (1993) 245–262, https://doi.org/10.1007/BF00766147.
[3] F. Boccuzzi, A. Chiorino, S. Tsubota, M. Haruta, FTIR study of carbon monoxide oxidation and scrambling at room temperature over gold supported on ZnO and TiO_2: 2, J. Phys. Chem. 100 (1996) 3625–3631, https://doi.org/10.1021/jp952259n.
[4] M. Dekkers, M. Lippits, B. Nieuwenhuys, CO adsorption and oxidation on Au/TiO_2, Catal. Lett. 56 (1998) 195–197, https://doi.org/10.1023/A:1019037902776.
[5] R.M. Finch, N.A. Hodge, G.J. Hutchings, A. Meagher, Q.A. Pankhurst, M.R. H. Siddiqui, F.E. Wagner, R. Whyman, Identification of active phases in Au–Fe catalysts for low-temperature CO oxidation, Phys. Chem. Chem. Phys. 1 (1999) 485–489, https://doi.org/10.1039/A808208A.
[6] A. Sanchez, S. Abbet, U. Heiz, W.-D. Schneider, H. Häkkinen, R. Barnett, U. Landman, When gold is not noble: nanoscale gold catalysts, J. Phys. Chem. A 103 (1999) 9573–9578, https://doi.org/10.1021/jp9935992.
[7] Y.-S. Su, M.-Y. Lee, S.D. Lin, XPS and DRS of Au/TiO_2 catalysts: effect of pretreatment, Catal. Lett. 57 (1999) 49–53, https://doi.org/10.1021/jp9935992.
[8] G.C. Bond, D.T. Thompson, Gold-catalysed oxidation of carbon monoxide, Gold Bull. 33 (2000) 41–50, https://doi.org/10.1007/BF03216579.
[9] F. Boccuzzi, A. Chiorino, M. Manzoli, P. Lu, T. Akita, S. Ichikawa, M. Haruta, Au/TiO_2 nanosized samples: a catalytic, TEM, and FTIR study of the effect of calcination temperature on the CO oxidation, J. Catal. 202 (2001) 256–267, https://doi.org/10.1006/jcat.2001.3290.
[10] C.H. Lin, S.H. Hsu, M.Y. Lee, S.D. Lin, Active morphology of $Au/\gamma\text{-}Al_2O_3$—a model by EXAFS, J. Catal. 209 (2002) 62–68, https://doi.org/10.1006/jcat.2002.3621.
[11] C. Costello, M. Kung, H.-S. Oh, Y. Wang, H.H. Kung, Nature of the active site for CO oxidation on highly active $Au/\gamma\text{-}Al_2O_3$, Appl. Catal. A Gen. 232 (2002) 159–168, https://doi.org/10.1016/S0926-860X(02)00092-3.
[12] M. Daté, Y. Ichihashi, T. Yamashita, A. Chiorino, F. Boccuzzi, M. Haruta, Performance of Au/TiO_2 catalyst under ambient conditions, Catal. Today 72 (2002) 89–94, https://doi.org/10.1016/S0920-5861(01)00481-3.
[13] T. Fujitani, I. Nakamura, A. Takahashi, H_2O dissociation at the perimeter interface between gold nanoparticles and TiO_2 is crucial for oxidation of CO, ACS Catal. 10 (2020) 2517–2521, https://doi.org/10.1021/acscatal.9b05195.
[14] M. Daté, M. Haruta, Moisture effect on CO Oxidation over Au/TiO_2 catalyst, J. Catal. 201 (2001) 221–224, https://doi.org/10.1006/jcat.2001.3254.
[15] M. Daté, M. Okumura, S. Tsubota, M. Haruta, Vital role of moisture in the catalytic activity of supported gold nanoparticles, Angew. Chem. Int. Ed. 43 (2004) 2129–2132, https://doi.org/10.1002/ange.200453796.
[16] M. Ojeda, B.-Z. Zhan, E. Iglesia, Mechanistic interpretation of CO oxidation turnover rates on supported Au clusters, J. Catal. 285 (2012) 92–102, https://doi.org/10.1016/j.jcat.2011.09.015.
[17] J. Saavedra, H.A. Doan, C.J. Pursell, L.C. Grabow, B.D. Chandler, The critical role of water at the gold-titania interface in catalytic CO oxidation, Science 345 (2014) 1599–1602, https://doi.org/10.1126/science.1256018.
[18] J. Saavedra, T. Whittaker, Z. Chen, C.J. Pursell, R.M. Rioux, B.D. Chandler, Controlling activity and selectivity using water in the Au-catalysed preferential oxidation of CO in H_2, Nat. Chem. 8 (2016) 584–589, https://doi.org/10.1038/nchem.2494.
[19] C. Costello, J. Yang, H. Law, Y. Wang, J.-N. Lin, L. Marks, M. Kung, H.H. Kung, On the potential role of hydroxyl groups in CO oxidation over Au/Al_2O_3, Appl. Catal. A Gen. 243 (2003) 15–24, https://doi.org/10.1016/S0926-860X(02)00533-1.
[20] P. Konova, A. Naydenov, C. Venkov, D. Mehandjiev, D. Andreeva, T. Tabakova, Activity and deactivation of Au/TiO_2 catalyst in CO oxidation, J. Mol. Catal. A Chem. 213 (2004) 235–240, https://doi.org/10.1016/j.molcata.2003.12.021.
[21] H. Kung, M. Kung, C. Costello, Supported Au catalysts for low temperature CO oxidation, J. Catal. 216 (2003) 425–432, https://doi.org/10.1016/S0021-9517(02)00111-2.
[22] S. Zhao, F. Chen, S. Duan, B. Shao, T. Li, H. Tang, Q. Lin, J. Zhang, L. Li, J. Huang, N. Bion, W. Liu, H. Sun, A.-Q. Wang, M. Haruta, B. Qiao, J. Li, J. Liu, T. Zhang, Remarkable active-site dependent H_2O promoting effect in CO oxidation, Nat. Commun. 10 (3824) (2019) 1–9, https://doi.org/10.1038/s41467-019-11871-w.
[23] E. Gulari, C. Güldür, S. Srivannavit, S. Osuwan, CO oxidation by silver cobalt composite oxide, Appl. Catal. A Gen. 182 (1999) 147–163, https://doi.org/10.1016/S0926-860X(99)00002-2.
[24] T.-M. Tran-Thuy, C.-C. Chen, S.D. Lin, Spectroscopic studies of how moisture enhances CO oxidation over Au/BN at ambient temperature, ACS Catal. 7 (2017) 4304–4312, https://doi.org/10.1021/acscatal.7b01374.
[25] S.-E. Fu, C.-H. Yeh, P.-J. Lin, S. Nachimuthu, J.-C. Jiang, A first principles study of CO oxidation over gold clusters: the catalytic role of boron nitride support and water, Mol. Catal. 471 (2019) 44–53, https://doi.org/10.1016/j.mcat.2019.04.015.
[26] C. Sivadinarayana, T.V. Choudhary, L.L. Daemen, J. Eckert, Goodman, D. W. Goodman, The nature of the surface species formed on Au/TiO_2 during the reaction of H_2 and O_2: an inelastic neutron scattering study, J. Am. Chem. Soc. 126 (2004) 38–39, https://doi.org/10.1021/ja0381398.
[27] J. Saavedra, C.J. Pursell, B.D. Chandler, CO oxidation kinetics over Au/TiO2 and Au/Al_2O_3 catalysts: evidence for a common water-assisted mechanism, J. Am. Chem. Soc. 140 (2018) 3712–3723, https://doi.org/10.1021/jacs.7b12758.
[28] J. Thomas, N. Weston, T. O'connor, Turbostratic boron nitride, thermal transformation to ordered-layer-lattice boron nitride, J. Am. Chem. Soc. 84 (1962) 4619–4622, https://doi.org/10.1021/ja00883a001.
[29] G. Bergeret, P. Gallezot. Particle Size and Dispersion Measurements. Handbook of Heretogeneous Catalysis, Wiley-VCH, 2008, pp. 738–765, https://doi.org/10.1002/9783527610044.hetcat0038.
[30] X.D. Luong, T. Ishida, A. Taketoshi, D.Q. Truong, D.C. Huynh, T. Honma, T. Murayama, M. Haruta, Supported gold cluster catalysts prepared by solid grinding using a non-volatile organogold complex for low-temperature CO oxidation and the effect of potassium on gold particle size, Appl. Catal. B 241 (2019) 539–547, https://doi.org/10.1016/j.apcatb.2018.09.053.
[31] M. Okumura, S. Nakamura, S. Tsubota, T. Nakamura, M. Azuma, M. Haruta, Chemical vapor deposition of gold on Al_2O_3, SiO_2, and TiO_2 for the oxidation of CO and of H_2, Catal. Lett. 51 (1998) 53–58, https://doi.org/10.1023/A:1019020614336.
[32] M.J. Kahlich, H.A. Gasteiger, R.J. Behm, Kinetics of the selective low-temperature oxidation of CO in H_2-rich gas over $Au/\alpha\text{-}Fe_2O_3$, J. Catal. 182 (1999) 430–440, https://doi.org/10.1006/jcat.1998.2333.
[33] M. Haruta, Nanoparticulate gold catalysts for low-temperature CO oxidation, J. New Mater. Electrochem. Syst. 7 (2004) 163–172, https://doi.org/10.1002/chin.200448226.
[34] M. Haruta, Gold as a novel catalyst in the 21st century: preparation, working mechanism and applications, Gold Bull. 37 (2004) 27–36, https://doi.org/10.1007/BF03215514.
[35] A. Ivanova, E. Slavinskaya, O. Stonkus, R. Gulyaev, T. Glazneva, A. Noskov, A. Boronin, Highly active and durable Pd/Fe_2O_3 catalysts for wet CO oxidation under ambient conditions, Catal. Sci. Technol. 6 (2016) 3918–3928, https://doi.org/10.1039/C5CY01588J.
[36] T. Morimoto, M. Nagao, F. Tokuda, Relation between the amounts of chemisorbed and physisorbed water on metal oxides, J. Phys. Chem. 73 (1969) 243–248, https://doi.org/10.1021/j100721a039.

[37] F. Boccuzzi, A. Chiorino, M. Manzoli, FTIR study of the electronic effects of CO adsorbed on gold nanoparticles supported on titania, Surf. Sci. 454 (2000) 942–946, https://doi.org/10.1016/S0039-6028(00)00160-6.
[38] M. Mihaylov, H. Knoezinger, K. Hadjiivanov, B.C. Gates, Characterization of the oxidation states of supported gold species by IR spectroscopy of adsorbed CO, Chem. Ing. Tech. 79 (2007) 795–806, https://doi.org/10.1002/cite.200700029.
[39] T. Venkov, K. Fajerwerg, L. Delannoy, H. Klimev, K. Hadjiivanov, C. Louis, Effect of the activation temperature on the state of gold supported on titania: an FT-IR spectroscopic study, Appl. Catal. A Gen. 301 (2006) 106–114, https://doi.org/10.1016/j.apcata.2005.11.019.
[40] L. Delannoy, N. Weiher, N. Tsapatsaris, A.M. Beesley, L. Nchari, S.L.M. Schroeder, C. Louis, Reducibility of supported gold (III) precursors: influence of the metal oxide support and consequences for CO oxidation activity, Top. Catal. 44 (2007) 263–273, https://doi.org/10.1007/s11244-007-0299-3.
[41] J. Wang, B. Hammer, Oxidation state of oxide supported nanometric gold, Top. Catal. 44 (2007) 49–56, https://doi.org/10.1007/s11244-007-0277-9.
[42] A. Jentys, Estimation of mean size and shape of small metal particles by EXAFS, Phys. Chem. Chem. Phys. 1 (1999) 4059–4063, https://doi.org/10.1039/A904654B.
[43] J. Miller, A. Kropf, Y. Zha, J. Regalbuto, L. Delannoy, C. Louis, E. Bus, J.A. V. Bokhoven, The effect of gold particle size on AuAu bond length and reactivity toward oxygen in supported catalysts, J. Catal. 240 (2006) 222–234, https://doi.org/10.1016/j.jcat.2006.04.004.
[44] N.S. Marinkovic, K. Sasaki, R.R. Adzic, Determination of single-and multi-component nanoparticle sizes by X-ray absorption spectroscopy, J. Electrochem. Soc. 165 (2018) J3222–J3230, https://doi.org/10.1149/2.0281815jes.
[45] R. Quiller, T. Baker, X. Deng, M. Colling, B. Min, C. Friend, Transient hydroxyl formation from water on oxygen-covered Au (111), J. Chem. Phys. 117 (2008) 17319–17326, https://doi.org/10.1063/1.2965821.
[46] M.A. Bollinger, M.A. Vannice, A kinetic and DRIFTS study of low-temperature carbon monoxide oxidation over Au-TiO_2 catalysts, Appl. Catal. B 8 (1996) 417–443, https://doi.org/10.1016/0926-3373(96)90129-0.
[47] H.K. Livingston, Cross-sectional areas of molecules adsorbed on solid surfaces1a, J. Am. Chem. Soc. 66 (1944) 569–573, https://doi.org/10.1021/ja01232a021.
[48] Y. Lei, S. Pakhira, K. Fujisawa, H. Liu, C. Guerrero-Bermea, T. Zhang, A. Dasgupta, L.M. Martinez, S.R.O. Singamaneni, K. Wang, J. Shallenberger, A.L. Elías, R. Cruz-Silva, M. Endo, J.L. Mendoza-Cortes, M. Terrones, Low temperature activation of inert hexagonal boron nitride for metal deposition and single atom catalysis, Mater. Today 51 (2021) 108–116, https://doi.org/10.1016/j.mattod.2021.09.017.
[49] S. Banerjee, C. Majumder, Stability and electronic properties of Au atom doped hexagonal boron nitride sheet on Ni(111) support: role of vacancy defects and supports towards single atom catalysis, Appl. Surf. Sci. 515 (2020), 145978, https://doi.org/10.1016/j.apsusc.2020.145978.
[50] Q. Cai, D. Scullion, A. Falin, K. Watanabe, T. Taniguchi, Y. Chen, E.J.G. Santos, L. H. Li, Raman signature and phonon dispersion of atomically thin boron nitride, Nanoscale 9 (2017) 3059–3067, https://doi.org/10.1039/C6NR09312D.
[51] A.M. Kovalskii, I.N. Volkov, N.D. Evdokimenko, O.P. Tkachenko, D.V. Leybo, I. V. Chepkasov, Z.I. Popov, A.T. Matveev, A. Manakhov, E.S. Permyakova, A. S. Konopatsky, A.L. Kustov, D.V. Golberg, D.V. Shtansky, Hexagonal BN-and BNO-supported Au and Pt nanocatalysts in carbon monoxide oxidation and carbon dioxide hydrogenation reactions, Appl. Catal. B 303 (2022), 120891, https://doi.org/10.1016/j.apcatb.2021.120891.
[52] B. Zhong, T. Zhang, X.X. Huang, G.W. Wen, J.W. Chen, C.J. Wang, Y.D. Huang, Fabrication and Raman scattering behavior of novel turbostratic BN thin films, Mater. Lett. 151 (2015) 130–133, https://doi.org/10.1016/j.matlet.2015.03.059.
[53] W. Auwärter, Hexagonal boron nitride monolayers on metal supports: versatile templates for atoms, molecules and nanostructures, Surf. Sci. Rep. 74 (2019) 1–95, https://doi.org/10.1016/j.surfrep.2018.10.001.
[54] D. Roy, K. Panigrahi, B.K. Das, U.K. Ghorui, S. Bhattacharjee, M. Samanta, S. Sarkar, K. Chattopadhyay, Boron vacancy: a strategy to boost the oxygen reduction reaction of hexagonal boron nitride nanosheet in hBN-2H-MoS2 heterostructure, Nanoscale Adv. 3 (2021) 4739–4749, https://doi.org/10.1039/D1NA00304F.